nature materials

ARTICLES

https://doi.org/10.1038/s41563-021-00965-w

Development of a photoelectrochemically self-improving Si/GaN photocathode for efficient and durable H_2 production

Guosong Zeng[1], Tuan Anh Pham[2], Srinivas Vanka[3], Guiji Liu[1], Chengyu Song[4], Jason K. Cooper[1], Zetian Mi[3]✉, Tadashi Ogitsu[2]✉ and Francesca M. Toma[1]✉

Development of an efficient yet durable photoelectrode is of paramount importance for deployment of solar-fuel production. Here, we report the photoelectrochemically self-improving behaviour of a silicon/gallium nitride photocathode active for hydrogen production with a Faradaic efficiency approaching ~100%. By using a correlative approach based on different spectroscopic and microscopic techniques, as well as density functional theory calculations, we provide a mechanistic understanding of the chemical transformation that is the origin of the self-improving behaviour. A thin layer of gallium oxynitride forms on the side walls of the gallium nitride grains, via a partial oxygen substitution at nitrogen sites, and displays a higher density of catalytic sites for the hydrogen-evolving reaction. This work demonstrates that the chemical transformation of gallium nitride into gallium oxynitride leads to sustained operation and enhanced catalytic activity, thus showing promise for oxynitride layers as protective catalytic coatings for hydrogen evolution.

Photoelectrochemical (PEC) water splitting mimics plants to generate sustainable clean fuels using two of the most abundant resources on earth—sunlight and water[1]. One prevailing scheme to attain this solar to chemical energy conversion artificially is to monolithically integrate a semiconductor material with electrocatalysts in a photoelectrode. In this approach, while the semiconductor efficiently collects the solar energy, the electrocatalyst, which sometimes also acts as a protection layer, lowers the overpotential, mediates the charge carrier transfer and provides active sites for the chemical reaction at the solid/liquid interface[2]. However, a typical conundrum in this field is related to the fact that efficient photoabsorbers are not durable (for example, Si and III–V photoelectrodes), whereas durable materials show poor efficiency (for example, TiO_2 and $SrTiO_3$)[2–4]. Thus, it is critically necessary to develop overlayers with a conduction (valence) band that is well aligned with otherwise efficient but unstable semiconductor photocathodes (photoanodes) to enable sustained and efficient operation[5]. Among many efficient yet unstable light absorbers, Si is a low-cost and earth-abundant material with a suitable band gap to absorb in the visible range, and with high charge carrier mobility. All these properties motivate the search for a stable coating to yield stable photoelectrodes. These coatings are usually a combination of a charge transport layer combined with a catalyst, thus promoting efficient charge collection and separation, and preventing corrosion. Different oxide[6–10], nitride[2,11], selenide[12] and sulfide[13] materials have been explored for protection of Si-based photocathodes, reaching several hundred hours stability in the presence of hydrogen evolution reaction (HER) catalysts. Among these, gallium nitride (GaN) is an interesting option due to the chemically stable nature of N-rich surfaces[14]. GaN can be particularly suitable as an efficient protective layer for the silicon photocathode due to the almost ideal conduction band alignment of these two materials for providing optimal electron transport[11,14]. While GaN has already been used in architectures with Si and Pt, or other electrocatalysts exposed to the electrolyte, less attention has been devoted to fundamental understanding of the Si/GaN architectures. The origin of their long-term stability, either via an intermediate-related self-healing effect[15–17], or pertaining to their thermodynamically stable nature[18], still remains unclear. Thus, there is a need to understand the fundamental aspects of GaN overlayers for ultimate optimization of PEC cell performance[6,19].

Herein, we demonstrate that Si/GaN photocathodes can generate sustained hydrogen production with a Faradaic efficiency (FE) of ~100% without the use of any electrocatalyst. We also perform accelerated testing and demonstrate that the Si/GaN photocathode can sustain high current density under intensified, 3.5-suns illumination for more than 150 h. We observe that under operating conditions, the photocurrent density and onset potential of Si/GaN photocathodes self improve. Specifically, we utilize a suite of advanced characterization techniques and first-principles calculations to elucidate the origins of this self-improving behaviour. Under operating conditions, Si/GaN photocathodes are subjected to a chemical transformation at the GaN surface that provides protection and enhances the PEC performance by adding active catalytic sites for hydrogen evolution reactions. The protected Si photocathodes thus show a stability and FE without the use of any electrocatalysts, as the result of a beneficial chemical transformation. This study reveals a self-improving behaviour of the Si/GaN photocathode active for hydrogen production, and sets an investigation model for fundamental understanding of the pivotal role of chemical transformation in PEC water splitting. The knowledge gained from this work can provide feedback for further optimization of PEC devices.

[1]Chemical Sciences Division, Lawrence Berkeley National Laboratory, Berkeley, CA, USA. [2]Materials Science Division, Lawrence Livermore National Laboratory, Livermore, CA, USA. [3]Department of Electrical Engineering and Computer Science, University of Michigan, Ann Arbor, MI, USA. [4]National Center for Electron Microscopy, Molecular Foundry, Lawrence Berkeley National Laboratory, Berkeley, CA, USA. ✉e-mail: ztmi@umich.edu; ogitsu1@llnl.gov; fmtoma@lbl.gov

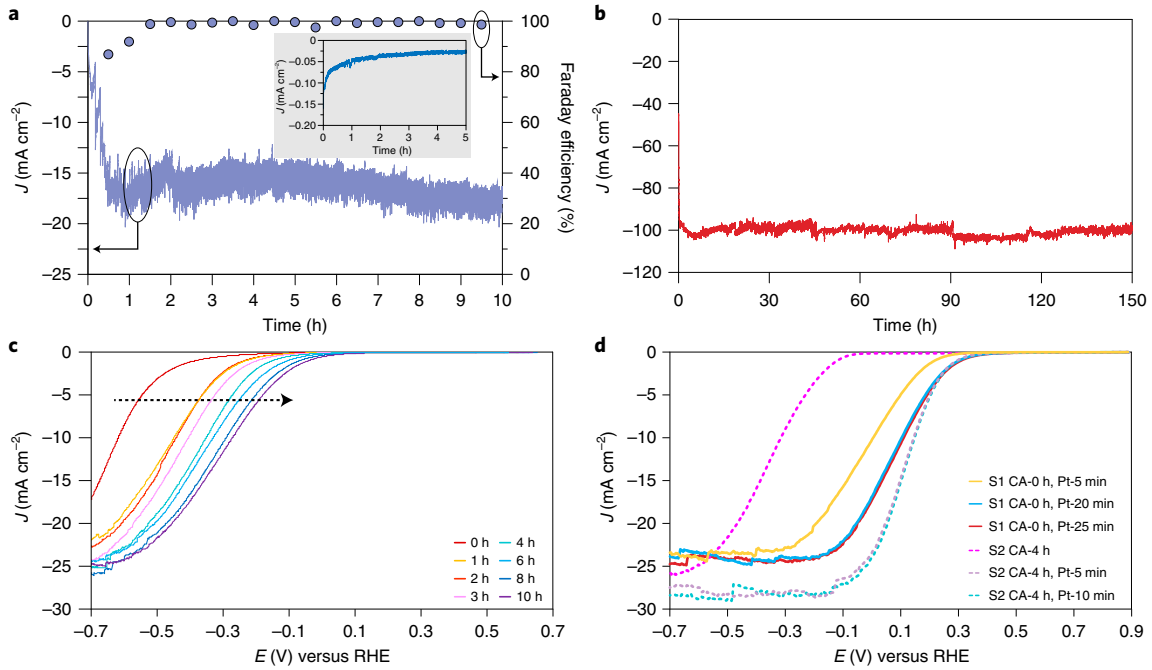

Fig. 1 | Self-improving behaviour of Si/GaN photocathodes. a, CA testing for 10 h under 1-sun illumination and constant bias at −0.6 V versus RHE, the corresponding Faradaic efficiency reveals the self-improving nature of GaN. Inset: CA testing on bare Si for 5 h under 1-sun illumination and −0.6 V versus RHE, this bare Si photocathode rapidly drops down to <0.05 mA cm^{-2} within an hour. **b**, Accelerated CA testing on bare epilayer Si/GaN photocathode at constant bias of −0.6 V versus RHE under 3.5-sun illumination for 150 h in 0.5 M H_2SO_4. **c**, Photocurrent density versus applied electrochemical potential (*J*–*E*) curves as a function of CA testing time. **d**, Several selected *J*–*E* curves of as-prepared Si/GaN photocathode (CA-0 h) and 4 h CA-tested Si/GaN photocathode (CA-4 h) with different Pt photodeposition durations under 1-sun illumination.

To set a baseline for understanding the stability mechanism of the GaN overlayer, Si/GaN photocathodes were investigated under water reduction conditions. IrO_x is used as the counter electrode and graphite colloidal adhesive is used to connect the Si/GaN to copper tape. This testing configuration prevents any metal contamination (Supplementary Fig. 1 and Methods). Chronoamperometric (CA) tests were conducted on different samples under 1-sun intensity illumination with a constant bias of −0.6 V versus the reverse hydrogen electrode (RHE), which is sufficient to drive the HER. In all different samples, the measured photocurrent undergoes an increase before it achieves a steady state. Interestingly, the calculated corresponding FE also follows a similar enhancement, that is, the FE starts at ~85% then achieves 100% once the photocurrent reaches its maximum (Fig. 1a and Supplementary Fig. 3a). Furthermore, Supplementary Fig. 3d verifies that only hydrogen and oxygen were produced during the CA testing. On the contrary, the bare n^+p silicon photocathode tested under the same testing conditions shows <0.1 mA cm^{-2} photocurrent density (Fig. 1a, inset). In addition, accelerated CA testing under an air mass (AM) 1.5 G solar illumination at an intensified 3.5-suns intensity was performed. While the photocurrent enhancement is still observed, this accelerated test further reveals that the Si/GaN photocathode can sustain >100 mA cm^{-2} photocurrent density for more than 150 h. This measurement demonstrates the stability of the Si/GaN photocathode at a high photocurrent value and under concentrated illumination conditions (Fig. 1b). So far, these photoelectrochemical characteristics are the best reported for protected Si photocathodes in the absence of a catalyst layer. Supplementary Table 1 summarizes the up-to-date recorded efficiencies, as well as the device stability of protected Si photocathodes.

To provide further insight into the PEC performance enhancement, we performed intermittent 10-h CA testing, with linear sweep voltammetry (LSV) collected after each hour to track the changes in PEC performance, that is, photocurrent density and onset potential. Interestingly, the photocurrent density versus applied potential (*J*–*E*) curve shows an anodic shift over time, with an onset potential shift of more than 300 mV, from −460 mV_{RHE} (as-prepared sample is denoted as CA-0 h) to −80 mV_{RHE} (sample tested for 10 h is denoted as CA-10 h), as shown in Fig. 1c and Supplementary Table 2. In addition, the maximum photocurrent density (*J*) gradually increases and reaches a saturation of 25 mA cm^{-2} after 3 h.

To look into the underlying mechanism of this self-improving behaviour, we first analysed the changes of the surface resistance by carrying out electrochemical impedance spectroscopy (EIS) at AM 1.5 G 1-sun illumination, which is reported as a Nyquist plot in Supplementary Fig. 3b. By evaluating the simulated equivalent circuit and the corresponding calculated results (inset Supplementary Fig. 3b and Supplementary Table 3), we observe that the surface resistance ($R_{ct,surf}$) decreases from 600 Ω to 100 Ω. The dramatic variation of $R_{ct,surf}$ evidences that the charge transfer at the solid/liquid interface improves over time. In addition, Mott–Schottky analysis reveals that the flat band potential is similar after reaction (Supplementary Fig. 4), which suggests that the flat band position is determined by the n^+p Si solar cell substrate, which is in agreement with previous results[11,20]. Given that the band alignment remains unchanged with a notable change in $R_{ct,surf}$ and mild changes in other resistance (*R*) and constant phase element values, we hypothesize that the observed self-improving behaviour originates from an improvement in the surface kinetics of the GaN layer.

The observed self-improving anodic shift of the onset potential and the charge transfer improvement indicate an enhanced catalytic activity of the PEC-tested GaN surface, which can usually be obtained through the integration of a catalyst layer. Therefore, with the unique opportunity of improving device performance while decreasing (noble metal) catalyst loading, we studied the direct integration of Pt catalyst onto the modified Si/GaN photocathode.

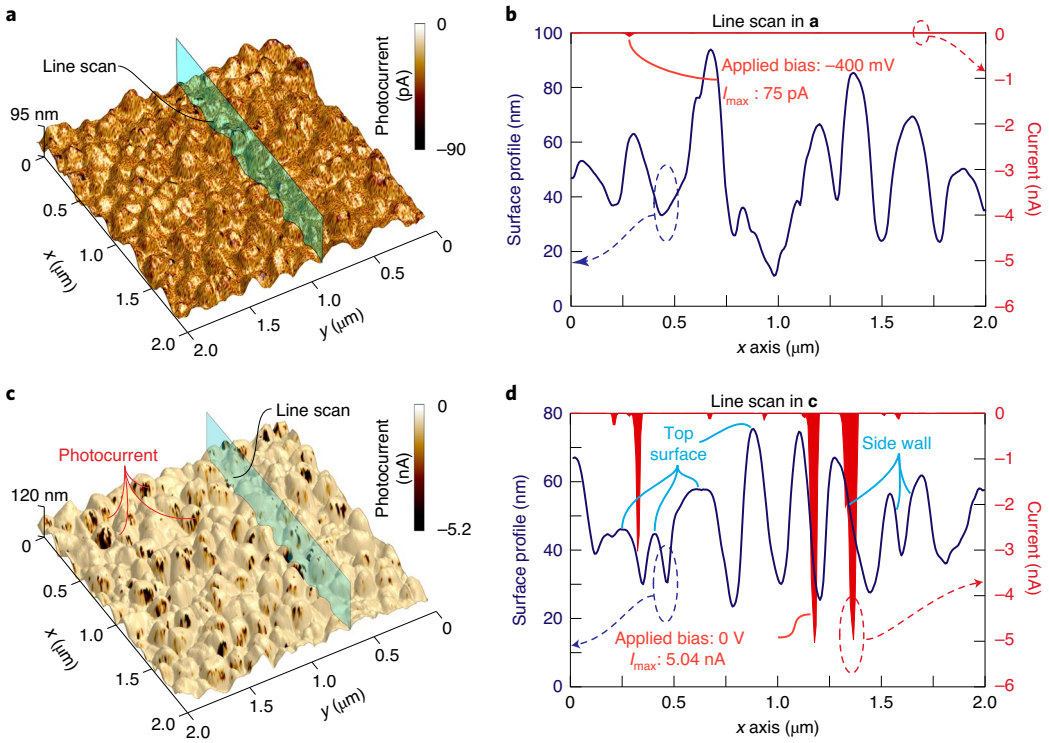

Fig. 2 | Photoconductive AFM characterization on CA-0 h and CA-10 h samples. a,**c**, The topography of the CA-0 h sample (**a**) and CA-10 h sample (**c**). **b**,**d**, Corresponding surface profile and photocurrent extracted from the line scans for the CA-0 h sample (**b**) and CA-10 h sample (**d**).

A comparison between the as-prepared Si/GaN photocathode and CA-tested surface was conducted. The initial PEC performance of the as-prepared sample was recorded by LSV scans. Then, the CA testing was carried out for 4 h to guarantee that the maximum current is achieved (Fig. 1a–c, improvement completes within the first few hours). Pt was photodeposited on both the as-prepared sample (denoted as S1 CA-0 h in Fig. 1d) and the 4-h CA-tested sample (denoted as S2 CA-4 h in Fig. 1d). As can be seen in Fig. 1d, the S2 CA-4 h sample only requires 5 min Pt deposition (S2 CA-4 h, Pt-5 min) to shift its turn-on voltage to 0.34 V, while an additional 5 min of Pt deposition (S2 CA-4 h, Pt-10 min) has a *J*–*E* curve that remains the same as for the 5 min deposition case. In stark contrast, 20 min of Pt deposition is needed to shift its turn-on voltage to 0.34 V (S1 CA-0 h, Pt-20 min), that is, the required Pt loading is four times higher than the CA-tested sample (full *J*–*E* curves versus Pt deposition duration in Supplementary Fig. 3c). This clearly proves that with such a CA-tested surface we can dramatically lower the use of platinum catalyst.

It is generally acknowledged that surface roughness change[21] and formation of new chemical species[13,17,22] are factors associated with the improvement of PEC performance. Thus, we performed atomic force microscopy (AFM) analysis, as well as scanning transmission electron microscopy combined with electron energy loss spectroscopy (STEM–EELS) and X-ray photoelectron spectroscopy (XPS), to trace the origin of the observed PEC performance enhancement. Specifically, by performing photoconductive AFM on both as-prepared (CA-0 h) and 10 h CA-tested (CA-10 h) samples, we compare the surface topography as well as probe the nanoscale origin of the macroscopic photocurrent enhancement. The surface morphology remains similar for CA-0 h and CA-10 h surfaces, with a similar surface roughness of about 12 nm (Fig. 2a,c), which rules out PEC performance improvement induced by surface roughness variation. However, we confirmed a substantial difference in the photocurrent of the CA-0 h and CA-10 h samples (Fig. 2). The overlaid topography–photocurrent maps (corresponding topography and photocurrent images are shown in Supplementary Figs. 5 and 6) show that the CA-0 h photocathode exhibits a maximum of ~80 pA at an applied bias −400 mV, whereas the CA-10 h photocathode exhibits a maximum of ~5 nA without the need of an external bias (Fig. 2b,d). The line profiles of the two maps for each sample highlight that the enhanced photocurrent generation in the tested sample is generated by the side walls of the grains, whereas the top of the grain barely contributes to the total photocurrent. We hypothesize that such location-dependent photocurrent generation may be associated with exposed facets and crystal orientation.

To understand how tested samples changed under operating conditions and the reason behind the increased photocurrent at the side wall of the GaN grains, state-of-the-art aberration correction STEM–EELS allows for analysis of crystal orientation combined with chemical information with <1 nm spatial resolution (Fig. 3a,b and Supplementary Fig. 7). An ~2-nm native oxide layer (highlighted in the white dashed line) is observed on the top surface of the grain for the CA-0 h sample, while less oxide (circled by a red dashed line) could be found on the side wall (Fig. 3a). Interestingly, after 10 h of operation, formation of an approximately 1-nm layer mixed with Ga, N and O at the side wall of the grain is observed (area surrounded by the red dashed line in Fig. 3b), while the top of the grain is covered with a Ga- and O-containing layer (no N is seen in the areas surrounded by the white dashed line in Fig. 3b) and no apparent change in the composition. Epitaxial GaN film possesses a wurtzite crystal structure, where the top surface of the grain is a polar *c* plane ($000\bar{1}$), while the side wall of the grain should be a mix of non-polar ($(10\bar{1}0)$ *m* plane and ($11\bar{2}0$) *a* plane and semi-polar planes (for example, ($11\bar{2}2$), ($20\bar{2}1$), etc.), as illustrated in Supplementary Fig. 8. Given that polarity and orientation effects of GaN often give rise to different chemical[23–25], electrical[26,27] and mechanical[28–30] responses to external stimulus, we can reasonably speculate that the accumulation of oxygen also has an orientation

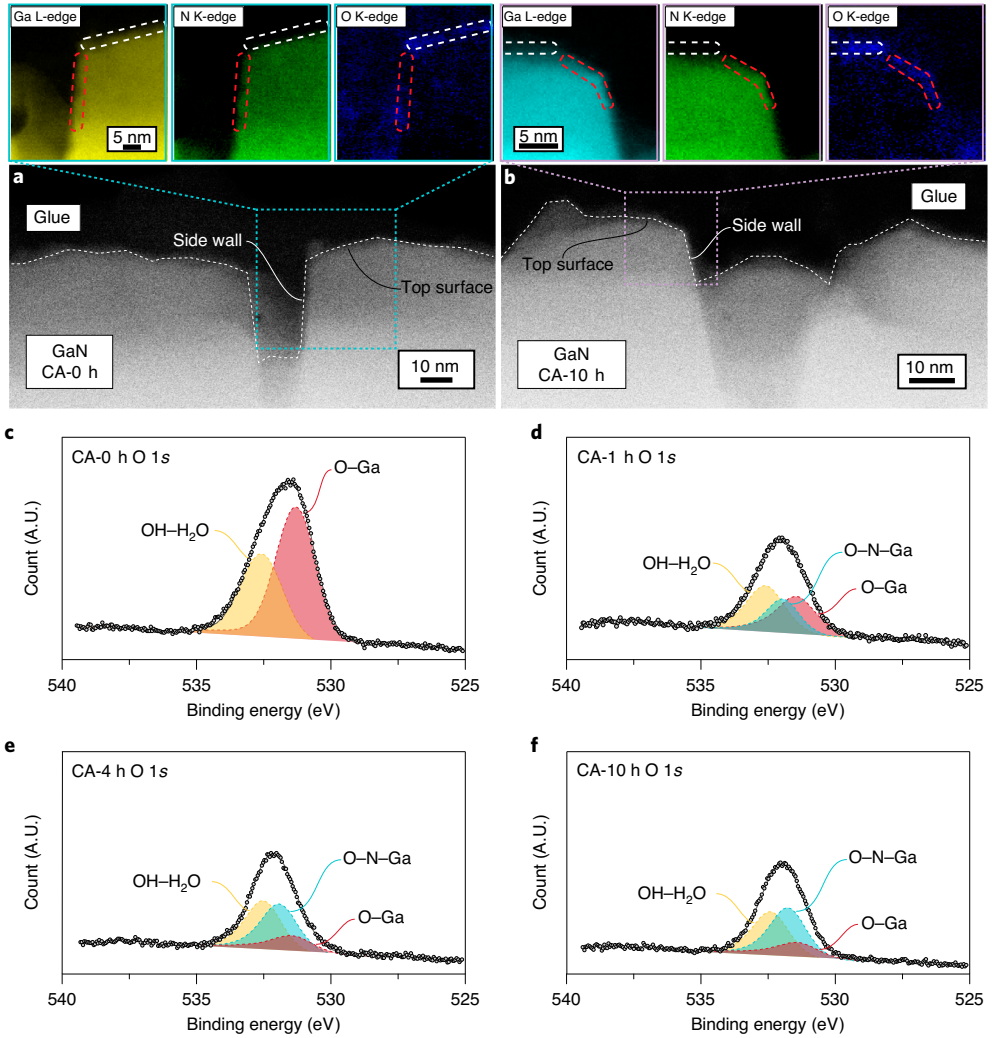

Fig. 3 | Chemical analysis of Si/GaN photocathode surface. a, STEM image of CA-0 h surface with insets (left to right) showing the EELS mappings of Ga L-edge, N K-edge and O K-edge. **b**, STEM image of CA-10 h surface with insets (left to right) showing the EELS mappings of Ga L-edge, N K-edge and O K-edge. **c**–**f**, O 1s core-level spectra of CA-0 h Si/GaN photocathode (**c**); Si/GaN photocathode after 1 h CA testing (**d**); Si/GaN photocathode after 4 h CA testing (**e**); and Si/GaN photocathode after 10 h CA testing (**f**).

preference, that is, forming on the non-polar or semi-polar planes (side wall of the grain) rather than on the polar *c* plane (top surface of the grain) is thermodynamically favoured.

By connecting the STEM–EELS results to the increased photocurrent and anodic shift of the onset potential (Figs. 1 and 2), we hypothesize the formation of an oxygen-containing GaN phase. This hypothesis was readily confirmed by XPS. In addition to the as-prepared sample, three different Si/GaN photocathodes were analysed after 1 h, 4 h and 10 h of chronoamperometric testing (CA-1 h, CA-4 h and CA-10 h). The XPS spectra of the as-prepared and tested samples show similar Ga 2*p* and N 1*s* core-level spectra and high signal-to-noise ratio, irrespective of the length of the test (Supplementary Fig. 9). In contrast, more insights are gained from O 1*s* spectra (Fig. 3c–f). In addition to OH-based and O–Ga–O species, by looking closer at the O 1*s* peaks, a new peak is emerging at 531.7 eV. This specific binding energy is assigned to gallium oxynitride[31,32]. Furthermore, compared to Ga 2*p* and N 1*s* spectra, the signal-to-noise ratio of the O 1*s* spectrum is substantially lower. Given that the probing depth of XPS for GaN is about 5–6 nm (ref. [33]), such a difference in signal-to-noise ratio (Fig. 3c–f and Supplementary Fig. 9) between O 1*s* and Ga 2*p* (or N 1*s*) suggests that all the samples are predominantly composed of GaN, while only an ultrathin layer of oxynitride presents at the surface. Altogether, these data support that such an oxynitride generates the considerable enhancement of the photocurrent generated at the side wall of the GaN grains (Fig. 2c), and is the key factor that leads to the self-improving behaviour.

To better understand how the experimental observation of the self-improving PEC performance, as well as the sustained operation of Si/GaN photocathodes, correlates to the presence of gallium oxynitride, we performed density functional theory (DFT) calculations for different GaN surfaces. We note that the top surface of our sample is $(000\bar{1})$, whereas the side wall of the grain consists of semi-polar and non-polar planes. For simplicity, our simulations were carried out for the $(000\bar{1})$ *c* plane and $(10\bar{1}0)$ *m* plane that represent the top and side wall of the system, respectively (see Supplementary Fig. 8 for GaN crystal structure).

First, to understand the role of oxygens on the stability of GaN, we considered several representative surface models and computed their formation energy (see Methods). For the $(000\bar{1})$ orientation, we found that a full replacement of nitrogen atoms of either surface or subsurface bilayers by oxygens (Fig. 4a, red and green lines) leads

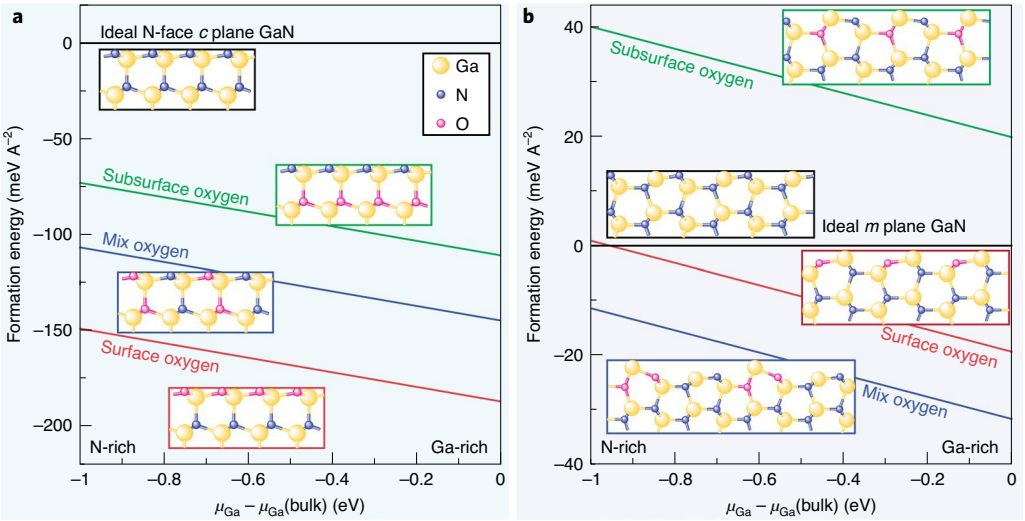

Fig. 4 | DFT calculation on N-polar *c* plane and non-polar *m* plane. a,**b**, Calculated formation energy of $(000\bar{1})$ *c* plane (**a**) and $(10\bar{1}0)$ *m* plane (**b**) GaN surfaces with different oxygen configuration within the anion- and cation-rich limits: ideal GaN surfaces of *c* plane and *m* plane; configurations with 100% replacement of nitrogen by oxygen on the surface *c* plane and *m* plane; 100% replacement of nitrogen by oxygen in the subsurface bilayer *c* plane and *m* plane; and configurations with 50% replacement of nitrogen of the surface and subsurface bilayers by oxygens *c* plane and *m* plane. In both cases, the ideal surface is chosen as the reference.

to a higher stability compared to the as-prepared surface. The same conclusion was achieved when nitrogen in these bilayers is simultaneously, but partly (50%), replaced by oxygen (Fig. 4a, blue line). Overall, we found that the configuration with all surface nitrogen substituted by oxygen exhibits the highest stability. This is consistent with previous studies[34] and current STEM results, which indicate a strong likelihood of forming an oxide layer on the topmost $(000\bar{1})$ surface.

Interestingly, our calculations show that the effect of oxygen substitution is rather different for the non-polar $(10\bar{1}0)$ surface. For this orientation, we found that the most stable structure is instead obtained by partial oxygen substitution (50%) of nitrogen in both surface and subsurface bilayers (Fig. 4b, blue line). A higher stability of this structure over the one with all the surface nitrogen replaced by oxygens (Fig. 4b, red line) is related to the ability to form surface Ga with a higher oxygen coordination (1.5 versus 1.0). Our calculations suggest that the topmost layers of the $(10\bar{1}0)$ orientation favour a mixture of all three species (Ga, O, N), in stark contrast to the $(000\bar{1})$ orientation, where they are more likely to consist of Ga and O only. This finding is in line with a previous study showing that surface charge localization and hopping can lead to the formation of N–O species and gallium oxynitride on the non-polar plane[24]. It also supports STEM–EELS evidence that the gallium oxynitride-like composition is more likely to form on the side wall of GaN grains.

Second, we move onto an assessment of catalytic activity. We base our descriptor on the free energy of adsorption of hydrogen, which is the key reaction intermediate for both the HER and hydrogen oxidation reaction. In particular, it has been suggested that the absolute magnitude of the free energy of hydrogen adsorption should be minimized to maximize the reaction ($|\Delta G_{ads}| \approx 0$). Here, examination of adsorption sites of the most stable surface of the non-polar plane (Fig. 4b, blue line) shows that $|\Delta G_{ads}|$ yields a value of 0.12–0.16 eV on Ga (Supplementary Fig. 10c,d), compared to a corresponding value of 1.07 eV obtained for the pristine surface (Supplementary Fig. 10a). On the other hand, N sites of the two surfaces yield a similar $|\Delta G_{ads}|$ of 0.31–0.39 eV (Supplementary Fig. 10b,e). The results show that the surface with partial nitrogen substitution by oxygens is more active than the pristine one, indicating that transformation in the surface composition is probably responsible for the improved performance of the GaN-protected photocathode.

To advance the application of solar water splitting for renewable energy, a tremendous amount of work has been applied to the development of cutting-edge coatings for long-term stability and high efficiency, whereas more effort needs to be focused on the fundamental study of the stability/degradation mechanisms of materials. In this work, we report Si/GaN photocathodes for sustained hydrogen production with 150 h stability under 3.5 suns and a ~100% FE without electrocatalyst. By employing state-of-the-art photoconductive AFM, STEM–EELS and XPS characterization techniques, we show the presence of a thin oxynitride-like layer, which forms over time on Si/GaN photocathodes within the first few hours of operation. Such gallium oxynitrides, as for other reported oxynitrides (TaON, HfON, perovskite oxynitride, etc.) that have hybridization of the N 2*p* and O 2*p* orbitals[35–39], possess better catalytic properties and perform a similar role in the electrocatalyst for better mediating charge transfer. The DFT simulation results were in line with experiments in which replacing the nitrogen atoms by oxygen to form oxynitride can passivate the surface for further stability, whereas the newly formed oxynitride can also provide more active sites for HER, leading to improved PEC performance. Comparing with other III–V semiconductor materials, which often suffer from photocorrosion issues[8,40], the findings from this work prove the uniqueness of GaN as a stable and efficient protective layer via formation of oxynitride during hydrogen production. This work also sets a prototype for fundamental understanding of the stability mechanism of protective layers in PEC water splitting applications, and the knowledge gained provides feedback for the development of further improved designs of durable and efficient photoelectrodes.

Online content

Any methods, additional references, Nature Research reporting summaries, source data, extended data, supplementary information, acknowledgements, peer review information; details of author contributions and competing interests; and statements of data and code availability are available at https://doi.org/10.1038/s41563-021-00965-w.

Received: 4 October 2020; Accepted: 19 February 2021;
Published online: 05 April 2021

References

1. Walter, M. G. et al. Solar water splitting cells. *Chem. Rev.* **110**, 6446–6473 (2010).
2. Vanka, S. et al. Long-term stability studies of a semiconductor photoelectrode in three-electrode configuration. *J. Mater. Chem. A* **7**, 27612–27619 (2019).
3. Hu, S. et al. Thin-film materials for the protection of semiconducting photoelectrodes in solar-fuel generators. *J. Phys. Chem. C* **119**, 24201–24228 (2015).
4. Khaselev, O. & Turner, J. A. A monolithic photovoltaic-photoelectrochemical device for hydrogen production via water splitting. *Science* **280**, 425–427 (1998).
5. Chen, L. et al. p-Type transparent conducting oxide/n-type semiconductor heterojunctions for efficient and stable solar water oxidation. *J. Am. Chem. Soc.* **137**, 9595–9603 (2015).
6. Scheuermann, A. G. et al. Design principles for maximizing photovoltage in metal-oxide-protected water-splitting photoanodes. *Nat. Mater.* **15**, 99–105 (2016).
7. Strandwitz, N. C. et al. Photoelectrochemical behavior of n-type Si(100) electrodes coated with thin films of manganese oxide grown by atomic layer deposition. *J. Phys. Chem. C* **117**, 4931–4936 (2013).
8. Hu, S. et al. Amorphous TiO_2 coatings stabilize Si, GaAs, and GaP photoanodes for efficient water oxidation. *Science* **344**, 1005–1009 (2014).
9. Fang, F. Z., Chen, Y. H., Zhang, X. D., Hu, X. T. & Zhang, G. X. Nanometric cutting of single crystal silicon surfaces modified by ion implantation. *CIRP Ann.* **60**, 527–530 (2011).
10. Gu, J. et al. A graded catalytic-protective layer for an efficient and stable water-splitting photocathode. *Nat. Energy* **2**, 16192 (2017).
11. Vanka, S. et al. High efficiency Si photocathode protected by multifunctional GaN nanostructures. *Nano Lett.* **18**, 6530–6537 (2018).
12. Huang, G. et al. Integrated $MoSe_2$ with n^+p-Si photocathodes for solar water splitting with high efficiency and stability. *Appl. Phys. Lett.* **112**, 013902 (2018).
13. King, L. A., Hellstern, T. R., Park, J., Sinclair, R. & Jaramillo, T. F. Highly stable molybdenum disulfide protected silicon photocathodes for photoelectrochemical water splitting. *ACS Appl. Mater. Interfaces* **9**, 36792–36798 (2017).
14. Kibria, M. G. et al. Atomic-scale origin of long-term stability and high performance of p-GaN nanowire arrays for photocatalytic overall pure water splitting. *Adv. Mater.* **28**, 8388–8397 (2016).
15. Lutterman, D. A., Surendranath, Y. & Nocera, D. G. A self-healing oxygen-evolving catalyst. *J. Am. Chem. Soc.* **131**, 3838–3839 (2009).
16. Malara, F., Fabbri, F., Marelli, M. & Naldoni, A. Controlling the surface energetics and kinetics of hematite photoanodes through few atomic layers of NiO_x. *ACS Catal.* **6**, 3619–3628 (2016).
17. Bergmann, A. et al. Reversible amorphization and the catalytically active state of crystalline Co_3O_4 during oxygen evolution. *Nat. Commun.* **6**, 8625 (2015).
18. Wang, D. et al. Wafer-level photocatalytic water splitting on GaN nanowire arrays grown by molecular beam epitaxy. *Nano Lett.* **11**, 2353–2357 (2011).
19. Toma, F. M. et al. Mechanistic insights into chemical and photochemical transformations of bismuth vanadate photoanodes. *Nat. Commun.* **7**, 12012 (2016).
20. He, Y. et al. Dependence of interface energetics and kinetics on catalyst loading in a photoelectrochemical system. *Nano Res.* **12**, 2378–2384 (2019).
21. Jiang, K. et al. Effects of surface roughness on the electrochemical reduction of CO_2 over Cu. *ACS Energy Lett.* **5**, 1206–1214 (2020).
22. Yang, J. et al. A multifunctional biphasic water splitting catalyst tailored for integration with high-performance semiconductor photoanodes. *Nat. Mater.* **16**, 335–341 (2017).
23. Bermudez, V. M. The fundamental surface science of wurtzite gallium nitride. *Surf. Sci. Rep.* **72**, 147–315 (2017).
24. Akimov, A. V., Muckerman, J. T. & Prezhdo, O. V. Nonadiabatic dynamics of positive charge during photocatalytic water splitting on GaN(10-10) surface: charge localization governs splitting efficiency. *J. Am. Chem. Soc.* **135**, 8682–8691 (2013).
25. Wang, J., Pedroza, L. S., Poissier, A. & Fernández-Serra, M. V. Water dissociation at the GaN($10\bar{1}0$) surface: structure, dynamics and surface acidity. *J. Phys. Chem. C* **116**, 14382–14389 (2012).
26. Stutzmann, M. et al. Playing with polarity. *Phys. Stat. Sol. B* **512**, 505–512 (2001).
27. Hellman, E. S. The polarity of GaN: a critical review. *MRS Internet J. Nitride Semicond. Res.* **3**, E11 (1999).
28. Zeng, G., Sun, W., Song, R., Tansu, N. & Krick, B. A. Crystal orientation dependence of gallium nitride wear. *Sci. Rep.* **7**, 14126 (2017).
29. Zeng, G., Tan, C. K., Tansu, N. & Krick, B. A. Ultralow wear gallium nitride. *Appl. Phys. Lett.* **109**, 051602 (2016).
30. Bernal, R. A. et al. Effect of growth orientation and diameter on the elasticity of GaN nanowires. A combined in situ TEM and atomistic modeling investigation. *Nano Lett.* **11**, 548–555 (2011).
31. Wolter, S. D. et al. X-ray photoelectron spectroscopy and X-ray diffraction study of the thermal oxide on gallium nitride. *Appl. Phys. Lett.* **70**, 2156 (1997).
32. Wolter, S. D., DeLucca, J. M., Mohney, S. E., Kern, R. S. & Kuo, C. P. An investigation into the early stages of oxide growth on gallium nitride. *Thin Solid Films* **371**, 153–160 (2000).
33. Zhao, Y. et al. Precise determination of surface band bending in Ga-polar n-GaN films by angular dependent X-ray photoemission spectroscopy. *Sci. Rep.* **9**, 16969 (2019).
34. Sun, Q., Selloni, A., Myers, T. H. & Doolittle, W. A. Oxygen adsorption and incorporation at irradiated GaN (0001) and GaN (000 1) surfaces: first-principles density-functional calculations. *Phys. Rev. B* **74**, 195317 (2006).
35. Wu, Y., Lazic, P., Hautier, G., Persson, K. & Ceder, G. First principles high throughput screening of oxynitrides for water-splitting photocatalysts. *Energy Environ. Sci.* **6**, 157–168 (2013).
36. Abe, R., Higashi, M. & Domen, K. Facile fabrication of an efficient oxynitride TaON photoanode for overall water splitting into H_2 and O_2 under visible light irradiation. *J. Am. Chem. Soc.* **132**, 11828–11829 (2010).
37. Yang, X. et al. Nitrogen-plasma treated hafnium oxyhydroxide as an efficient acid-stable electrocatalyst for hydrogen evolution and oxidation reactions. *Nat. Commun.* **10**, 1543 (2019).
38. Kreider, M. E. et al. Nitride or oxynitride? Elucidating the composition–activity relationships in molybdenum nitride electrocatalysts for the oxygen reduction reaction. *Chem. Mater.* https://doi.org/10.1021/acs.chemmater.9b05212 (2020).
39. Yang, M. et al. Anion order in perovskite oxynitrides. *Nat. Chem.* **3**, 47–52 (2011).
40. Lim, H. et al. High performance III–V photoelectrodes for solar water splitting via synergistically tailored structure and stoichiometry. *Nat. Commun.* **10**, 3388 (2019).

Methods

DFT simulations. The DFT calculations were performed with the generalized gradient approximation[41], using the plane-wave pseudopotential QUANTUM-ESPRESSO package[42]. Ultrasoft pseudopotentials were used to describe the interaction between valence electrons and ionic cores[43], where Ga 3*d* electrons were explicitly treated as valence electrons. The wavefunctions and electronic density were expanded in a plane-wave basis set truncated at a cut-off energy of 30 Ry and 240 Ry, respectively. The surface was modelled using a repeated slab geometry using a (2×2) unit cell with a thickness of seven GaN bilayers, where the Ga-terminated bottom side was passivated by pseudo-hydrogen with a charge of 1.25*e*. In addition, the (1010) surface was modelled using eight GaN atomic layers with a lateral dimension of 9.57 Å×10.38 Å. A vacuum width of at least 15.0 Å was introduced between consecutive slabs, and a k-point mesh of 5×5×1 and 2×2×1 was used to sample the surface Brillouin zone for the polar and non-polar surfaces, respectively.

The relative surface formation energies with respect to the pristine N face surface were computed as:

Here, A is the surface area, E_{total} is the total energy of the configuration under consideration, whereas E_{ref} is the total energy of the pristine N face surface. In addition, μ_i is the chemical potential of the ith species, and Δn_O, Δn_{Ga} and Δn_N are the excess or deficit of O, Ga and N atoms with respect to the reference, respectively. We assume that the surface was in equilibrium with bulk GaN, for example, $\mu_{Ga}+\mu_N=E_{GaN}$, where E_{GaN} is the total energy of bulk GaN. For oxygen, we focus on results of μ_O corresponding to the value in β-Ga_2O_3, that is, $2\mu_{Ga}+3\mu_O=|\Delta G_{ads}|$, where $E_{Ga_2O_3}$ is the total energy of the bulk β-Ga_2O_3, which was determined using a monoclinic unit cell containing 20 atoms (space group $C2/m$). In this way, the surface formation energy is a function of μ_{Ga}, which varies between $\mu_{Ga}(\text{bulk})+\Delta H(\text{GaN})\leq\mu_{Ga}\leq\mu_{Ga}(\text{bulk})$. Here, we obtained a value of $\Delta H(\text{GaN})=-1.0$ eV for the heat of formation (ΔH) of bulk GaN, in good agreement with previous studies[34].

Material growth. For this study, p-type 2-inch Si(100) double-sided polished wafers (from WRS Materials, thickness, 254–304 µm; resistivity, 1–10 Ω cm) were spin-coated (speed, 3,000 r.p.m; time, 20 s) with liquid phosphorous dopant precursor (from Futurrex) on one side to form the n^+-Si, and liquid boron dopant precursor (from Futurrex) on the other side to form the p^+-Si. Subsequently, the thermal diffusion process was conducted at 950 °C for 240 min under nitrogen gas flow in an AE Engineering tube furnace. After annealing, the precursor residue on the Si wafers was removed by soaking in buffered hydrofluoric acid (BHF) 10:1 solution (J. T. Baker) for 10 min and then rinsing with deionized water. The wafers were dried using a nitrogen gun. Further performance details of the Si solar cell substrates used in this study are discussed elsewhere[11]. A 100-nm n^+-GaN quasi-epilayer was grown on the n^+p Si substrates using a Veeco GEN II radio frequency plasma-assisted molecular beam epitaxial (PA-MBE) growth system. Before the growth, Si wafers were cleaned using standard protocols with acetone/methanol/water and subsequently with 10:1 BHF solution[2,11]. Nitrogen-terminated thin GaN quasi-film on Si was grown for 30 min at a substrate temperature ~735 °C, Ga beam equivalent pressure of ~2.2×10^{-7} torr, Ge cell (n-type dopant) temperature of 1,050 °C, a nitrogen flow rate of 0.45 standard cubic centimetres per minute (sccm) and 350 W plasma power. From secondary ion mass spectroscopy measurements, the growth rate of films was ~220 nm h^{-1} and average Ge concentration was 2×10^{18} atoms per cubic centimetre.

Supplementary Fig. 2 shows the photoluminescence peak position of the as-grown GaN quasi-epilayer on Si at ~365 nm, consistent with the wurtzite form of GaN from previous reports[44]. The peak at ~386 nm corresponds to the cubic form of GaN, which is due to the low temperature growth step during the MBE growth on a lattice mismatch Si-(100) substrate[45]. The carrier lifetimes of the Si/GaN photocathode at 365 nm and 386 nm were ~0.13 ns. This value is in good agreement with previous measurements, which show group III nitride carrier lifetimes of <1 ns (ref. [46]). The electrical conductivity of N-terminated GaN is ~1–10 Ω^{-1} cm^{-1}, and has been previously studied[47]. The flat band position of the Si/GaN photocathode is between 0.4 and 0.55 eV versus RHE[11,20].

Working electrode preparation. The back side of the Si/GaN sample was etched using HF vapour for 2 min to remove the silicon oxide and the fluorine that was weakly bonding to the surface and which temporarily prevented the surface being oxidized during the sample transfer to the sputtering chamber. A thickness of 50 nm of Al and 300 nm of Au were sputtered onto the silicon side and annealed in a tube furnace backfilled with Ar at 450 °C for 10 min to form an ohmic contact. Then, a graphite colloidal adhesive (Ted Pella PELCO isopropanol-based graphite paint) was used to connect the Al/Au side to a copper foil.

Photoelectrochemical testing. *Continuous chronoamperometric testing.* The GaN/silicon photocathode was tested in a compression cell filled with 0.5 M H_2SO_4 electrolyte (pH 0.4). The test was performed by using a three-electrode photoelectrochemical cell configuration, with IrO_x as counter electrode and a saturated calomel electrode as the reference electrode. A 10-h chronoamperometric test was carried out at a constant bias of −0.6 V versus RHE. To exclude metal contamination as a possible cause of the observed photocurrent enhancement, three different counter electrodes (that is, platinum, IrO_x and carbon rod) were used for comparison. As shown in Supplementary Fig. 1a, the self-improving behaviour was observed irrespective of the counter electrode. A small amount of Pt was detected on the working electrode when using the Pt counter electrode (Supplementary Fig. 1b). However, no metal contamination was observed on the working electrode when running the measurements in the presence of a carbon rod or IrO_x counter electrode (Supplementary Fig. 1c). Interestingly, we found that Ag paste contaminated the working electrode even in the presence of a protective epoxide, as revealed by Supplementary Fig. 1d. Therefore, we used only a graphite colloidal adhesive as the conductive adhesive to connect copper tape to the sample. The temperature was checked every 2 h to guarantee that long-time continuous irradiation will not induce a large temperature increase, which usually contributes to the increase of catalytic activity of many semiconductor materials.

Intermittent chronoamperometric testing. LSV and EIS were performed before the CA test to record the initial PEC performance of the material. CA with a constant bias at −0.6 V versus RHE was then performed for 1 h, followed by another LSV and EIS to capture the PEC performance after 1-h of CA modification. This was process was repeated to continuously monitor the change in PEC performance up to 10 h of CA testing.

Hydrogen evolution reaction. Continuous 10-h CA testing under simulated AM 1.5 illumination and constant bias at −0.6 V versus RHE was conducted on four Si/GaN samples to confirm the repeatability. The gas products were analysed using a gas chromatograph (Agilent 7890A). The cycle time for each injection was 7.5 min. Calibration curves for H_2 were obtained with a three-point calibration curve at 100, 1,000 and 9,918 ppm. Dry N_2 carrier gas with a flow rate at 1 sccm was purged into the electrolyte and brought the gas products into the gas chromatograph[48].

Photoconductive AFM. Photoconductive AFM measurements were conducted on Si/GaN samples before (as-received, AR) and after 10 h of CA testing (modified surface, MS) using a commercial AFM system (Bruker Dimension Icon). PeakForce TUNA mode was used to acquire the morphology and current simultaneously. A PtIr conductive probe with spring constant of 2.8 N m^{-1} was used for the scanning. A white light source was used to illuminate the surface during the acquisition[49].

X-ray photoemission spectroscopy. Surface chemical composition and valence band structure of GaN were obtained by XPS on a Kratos Axis Ultra DLD system at a take-off angle of 0° relative to the surface normal. An Al Kα source ($h\nu=1{,}486.6$ eV) was used to excite the core-level electrons. A pass energy of 20 eV was used for the narrow scan of core levels and valence band spectra, and a step size of 0.05 eV and 0.025 eV, respectively. The spectral fitting was conducted using CasaXPS analysis software. The binding energy scales of all core levels were corrected to the N 1*s* of Ga–N bond at 397.8 eV (ref. [50]).

STEM–EELS spectroscopy. STEM and EELS measurements were conducted on a double-aberration-corrected TEAM I microscope at the National Center for Electron Microscopy, operating at an accelerating voltage of 300 kV. EELS mapping was collected on a Gatan Continuum K3 camera with a 120-pA probe current.

Data availability

The data that support the findings of this study are available at HydroGEN Data Hub (http://datahub.h2awsm.org/). Additional data reported in the Supplementary Information are available from the corresponding authors upon request. Source data for Figs. 1–4 are available at https://datahub.h2awsm.org/project/about/photoelectrochemically-self-improving-si-gan-photocathode.

References

41. Perdew, J. P., Burke, K. & Ernzerhof, M. Generalized gradient approximation made simple. *Phys. Rev. Lett.* **77**, 3865 (1996).
42. Giannozzi, P. et al. QUANTUM ESPRESSO: a modular and open-source software project for quantum simulations of materials. *J. Phys. Condens. Matter* **21**, 395502 (2009).
43. Vanderbilt, D. Soft self-consistent pseudopotentials in a generalized eigenvalue formalism. *Phys. Rev. B* **41**, 7892 (1990).
44. Zhou, B. et al. A GaN:Sn nanoarchitecture integrated on a silicon platform for converting CO_2 to HCOOH by photoelectrocatalysis. *Energy Environ. Sci.* **12**, 2842–2848 (2019).
45. Liu, R., Schaller, R., Chen, C. Q. & Bayram, C. High internal quantum efficiency ultraviolet emission from phase-transition cubic GaN integrated on nanopatterned Si(100). *ACS Photonics* **5**, 955–963 (2018).
46. Nguyen, H. P. T. et al. Breaking the carrier injection bottleneck of phosphor-free nanowire white light-emitting diodes. *Nano Lett.* **13**, 5437–5442 (2013).
47. Chuah, L. S., Hassan, Z., Ng, S. S. & Hassan, H. A. High carrier concentrations of n- and p-doped GaN on Si(111) by nitrogen plasma-assisted molecular-beam epitaxy. *J. Mater. Res.* **22**, 2623–2630 (2007).

48. Kistler, T. A. et al. Integrated membrane-electrode-assembly photoelectrochemical cell under various feed conditions for solar water splitting. *J. Electrochem. Soc.* **166**, H3020–H3028 (2019).
49. Chen, R., Fan, F., Dittrich, T. & Li, C. Imaging photogenerated charge carriers on surfaces and interfaces of photocatalysts with surface photovoltage microscopy. *Chem. Soc. Rev.* **47**, 8238–8262 (2018).
50. Zhang, X. & Plasinska, S. Electronic and chemical structure of the H_2O/GaN(0001) interface under ambient conditions. *Sci. Rep.* **6**, 24848 (2016).

Acknowledgements

We gratefully acknowledge research support from the HydroGEN Advanced Water Splitting Materials Consortium, established as part of the Energy Materials Network under the US Department of Energy, Office of Energy Efficiency and Renewable Energy, Hydrogen and Fuel Cell Technologies Office, under contract no. DE-AC02-05CH11231 for Lawrence Berkeley National Laboratory, under contract no. DE-EE0008086 for the University of Michigan. Part of the work was performed under the auspices of the US Department of Energy by Lawrence Livermore National Laboratory under contract no. DE-AC52-07NA27344. Work at the Molecular Foundry was supported by the Office of Science, Office of Basic Energy Sciences, of the US Department of Energy under contract no. DE-AC02-05CH11231. We thank N. Danilovic, A. K. Buckley, J. L. Young, H. Li, D. Wang, R. Chen and Y. He for insightful discussions. We would also like to acknowledge the HydroGEN EMN data team, led by the National Renewable Energy Laboratory (NREL), for their assistance in reviewing the uploaded data and metadata to the Data Hub repository, making it public and obtaining the DOIs for the data. The HydroGEN Data Hub (https://datahub.h2awsm.org/) combines experimental and computational data into a searchable water splitting materials data infrastructure and distributes data to the scientific community and the public.

Author contributions

F.M.T., Z.M. and T.O. conceived the idea. F.M.T. supervised the work. G.Z. conducted the PEC testing, pc-AFM and XPS measurements. G.Z. and F.M.T. analysed and interpreted the results. J.K.C. helped with XPS experiment design and data interpretation. S.V. synthesized the material and conducted intensified stability tests. T.A.P. and T.O. performed the DFT calculations. G.L. and C.S. conducted the STEM–EELS experiments. G.Z., T.A.P. and F.M.T. wrote the manuscript. All of the authors contributed to the final version of the manuscript.

Competing interests

Some intellectual property related to the synthesis of GaN nanowires was licensed to NS Nanotech Inc., which was co-founded by Z.M.

Additional information

Supplementary information The online version contains supplementary material available at https://doi.org/10.1038/s41563-021-00965-w.

Correspondence and requests for materials should be addressed to Z.M., T.O. or F.M.T.

Peer review information *Nature Materials* thanks Nathan Neale, Yuan Ping and the other, anonymous, reviewer(s) for their contribution to the peer review of this work.